

Technology-Aware Simulation for Prototyping Molecular Field-Coupled Nanocomputing

Federico Ravera , Student Member, IEEE, Yuri Ardesi , Member, IEEE, Gianluca Piccinini , and Mariagrazia Graziano 

Abstract—The molecular Field-Coupled Nanocomputing (molFCN) paradigm encodes digital information in the charge distribution of molecules. The information propagates through electrostatic coupling within molecules, permitting minimal power consumption. Although the promising results in the design of molFCN circuits, a prototype is missing. Therefore, this work moves toward molFCN fabrication by presenting a methodology combining Finite Element Modelling with the SCERPA tool, boosting the simulation accuracy by considering both molecule and device physics. First, this work analyzes nano-trench-based molFCN single-line wires, examining information propagation dependencies on the nano-trench geometries. Then, the analysis of nano-trench-based multi-line wires points out the primary prototype specification to achieve this advantageous molFCN solution. Finally, we demonstrate the nano-trench as a valuable solution to achieve the write-in mechanism. Overall, this paper paves the way for molFCN fabrication-aware simulations for future prototyping.

Index Terms—Molecular electronics, design methodology, field-coupled nanocomputing.

I. INTRODUCTION & BACKGROUND

THE molecular Field-Coupled Nanocomputing (molFCN) technology implements the Quantum-dot Cellular Automata (QCA) paradigm by encoding logic information in the charge distribution of molecules [1]. Among the molecules proposed for molFCN implementation [2], [3], [4], this work uses the bis-ferrocene, which has been extensively analyzed in the molFCN context [5], [6]. Fig. 1(a) reports the bis-ferrocene, highlighting the functional groups, called dots, where charges can be localized [5]. Charges move in the molecules because of electrostatic coupling with neighboring molecules (E_{sw}) and the clock field (E_{ck}). Fig. 1(b) shows two electrostatically coupled bis-ferrocenes forming the molFCN unit cell. Charges move within dots to minimize Coulomb's repulsion, leading to the two minimum energy configurations that encode the

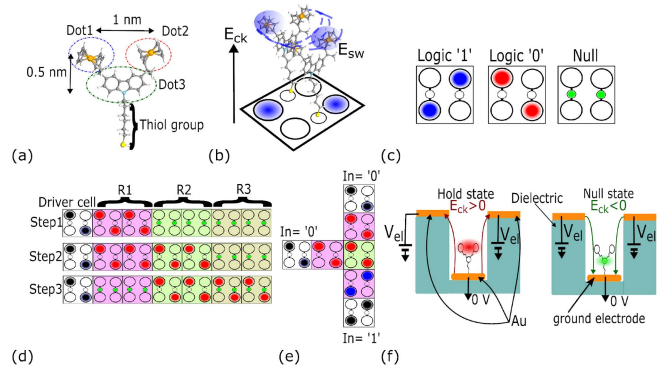


Fig. 1. (a) Bis-ferrocene structure and dots definition. (b) Unit cell definition and electrostatic coupling in two bis-ferrocene molecules. (c) Logic values definition in molFCN. (d) molFCN wire and MV with clock regions division. The information propagates by the successive activation of the regions. (e) Layout of a molFCN majority voter. (f) The nano-trench solution proposed in [18]. Positive and negative voltages on the electrodes force molecules into Null and Hold states, respectively.

logic values, as shown by Fig. 1(c), and enabling information propagation. Moreover, Fig. 1(b) shows E_{ck} vertically applied along the molecules. Positive E_{ck} pushes charges toward Dot1 and Dot2, creating the so-called hold state, which makes encoding possible. Oppositely, negative E_{ck} forces charge in Dot3, permitting the Null state, i.e., deleting encoded information. Fig. 1(d) reports a wire obtained by placing several cells on specific layouts [1]. The layout divides into clock regions R1, R2, and R3, controlled by different E_{ck} , which guides propagation starting from the fixed charge distribution of a driver cell and permits pipelining [7], [8]. The electrostatic repulsion also permits digital elaboration. Fig. 1(e) shows a Majority Voter (MV) implemented in molFCN technology. The information propagation is managed through electrostatic interactions, avoiding current flow and thus making molFCN an exciting beyond-CMOS solution [9], [10]. Moreover, molFCN theoretically permits THz frequencies and room temperature operations [11], [12]. Indeed, charge localization and electron transfer rates have been demonstrated to be weakly dependent on temperature-related effects in molFCN candidate molecules [12], [13]. Therefore, molFCN promises to overcome challenges presented in different QCA technological implementations, such as the need for cryogenic temperatures, thermal noise influence and MHz-limited switching capabilities [14], [15], [16], [17].

Despite the promising characteristics of molFCN, research is still pursuing a prototype, which must be addressed both from a

Manuscript received 3 May 2024; accepted 12 June 2024. Date of publication 18 June 2024; date of current version 28 June 2024. The review of this article was arranged by Associate Editor Y. Hirai. (Corresponding author: Federico Ravera.)

Federico Ravera, Yuri Ardesi, and Gianluca Piccinini are with the Department of Electronics and Telecommunications, Politecnico di Torino, 10129 Turin, Italy (e-mail: federico.ravera@polito.it; yuri.ardesi@polito.it; gianluca.piccinini@polito.it).

Mariagrazia Graziano is with the Department of Applied Science and Technology, Politecnico di Torino, 10129 Turin, Italy (e-mail: mariagrazia.graziano@polito.it).

This article has supplementary downloadable material available at <https://doi.org/10.1109/TNANO.2024.3415790>, provided by the authors.

Digital Object Identifier 10.1109/TNANO.2024.3415790

fabrication and a simulation perspective. Concerning the fabrication, molFCN devices require extremely precise nanopatterning, and the recent technological advances provide interesting fabrication possibilities, such as nanometric scale lithography and selective deposition techniques [19], [20], [21], [22], [23]. Nevertheless, the circuit-level analysis of molFCN lacks device- and fabrication-physics-aware considerations permitting structures evaluation already demonstrated effective for other QCA technologies, such as silicon dangling bonds [24]. In particular, linking the E_{ck} generation to molFCN circuit behavior would increase the propagation analysis accuracy. Therefore, considering the nano-trench solution proposed in [18] and reported in Fig. 1(f), this article delivers a framework enabling circuit investigation considering device and molecule physics. The nano-trench consists of a dielectric material with gold forming the ground and top electrodes. Bis-ferrocenes are eventually patterned on the ground electrode, taking advantage of the sulfur-gold chemistry [25]. The top electrode voltages (V_{el}) generate the needed E_{ck} for the Hold and Null states. We analyze different structures with Finite Element Modelling (FEM) based on the nano-trench solution, extracting the E_{ck} . The Self-Consistent Electrostatic Potential Algorithm (SCERPA) uses the E_{ck} fields to evaluate information propagation, linking structural parameters to circuit functioning.

This work is an initial step toward molFCN prototyping. It enhances simulation accuracy, eventually facilitating the definition of requirements and prototyping pathways.

II. METHODS

This work relies on the MoSQuiTo (Molecular Simulator Quantum-dot cellular automata Torino) methodology [6], consisting of three steps: molecules characterization, figures of merit definition, and circuit-level analysis. First, *ab initio* simulations derive relevant molecule electrostatic characteristics. Then, all the elaborated data are processed to extract figures of merit defining the molecule as an electronic device [6]. In particular, the Voltage-to-Aggregated Charge Transcharacteristic (VACT) relates the input voltage V_{in} , applied between Dot1 and Dot2 and derived from neighboring molecules charge distribution, to the sum of charges in the molecular dots, i.e., the Aggregated Charges (AC). The VACT is obtained under specific clock field conditions [8]. Fig. 2(a) schematizes the V_{in} and the AC definition, whereas Fig. 2(b) shows the bis-ferrocene cation VACTs evaluated for $E_{ck} = +2 \text{ V/nm}$, $E_{ck} = -2 \text{ V/nm}$ and $E_{ck} = 0 \text{ V/nm}$. The maximum charge separation is obtained by applying $E_{ck} = +2 \text{ V/nm}$. Supplementary Information (SI) material proposes detailed numerical relationships between the applied E_{ck} and the charge on the bis-ferrocene dots on a molFCN unit cell. Specifically, Fig. 1 in SI reports the behavior of the charge in the molecule dots for different E_{ck} values when either Logic ‘0’ or ‘1’ is applied. Moreover, Tables I and II in the SI report the numerical values of the AC in each dot of the molFCN unit cell. Then, the SCERPA tool evaluates molecular interactions by iteratively calculating the V_{in} for each molecule and associating the corresponding AC using the VACT [8], [18], [26]. Specifically, the SCERPA algorithm currently follows the

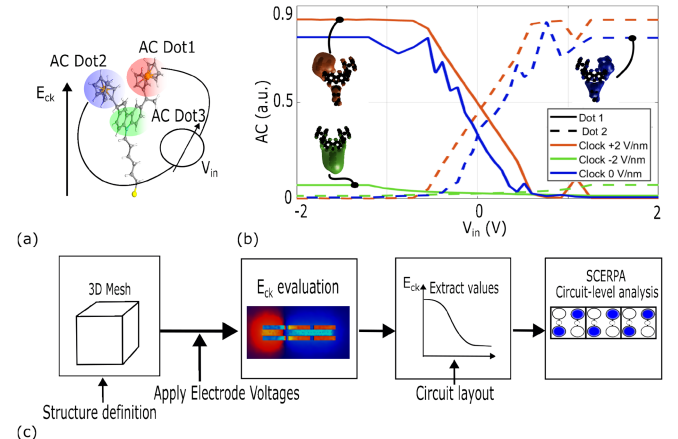


Fig. 2. (a) Schematic definition of V_{in} and the AC. (b) VACTs of the bis-ferrocene cation under $E_{ck} = +2 \text{ V/nm}$, $E_{ck} = -2 \text{ V/nm}$ and $E_{ck} = 0 \text{ V/nm}$. (c) Schematic flow diagram proposed in this work. The device mesh is calculated, and V_{el} are applied to extract the electric fields used for propagation analysis in SCERPA.

TABLE I
VOLTAGES APPLIED TO R1, R2, AND R3

Region	Electrode Voltage V_{el}			
	P1	P2	P3	P4
R1	-8 V	-8 V	+10 V	+8 V
R2	+10 V	-4 V	-4 V	+8 V
R3	+10 V	+12 V	-6 V	-6 V

TABLE II
GEOMETRICAL PARAMETERS OF THE SIMULATED CONFIGURATIONS

Conf.	D_s (nm)	T_w (nm)	W_{bot} (nm)	H_t (nm)	W_{top} (nm)	L_{el} (nm)
ConfA	2	3	2	6	2	10
ConfB	4	3	2	6	2	10
ConfB1	6	3	2	6	2	10
ConfC	2	4	3	6	2	10
ConfD	2	4	3	7	2	10
ConfE	2	4	3	7	6	10
ConfF	2	4	3	12	6	10
ConfG	2	4	3	17	6	10
ConfH	2	3	2	3	2	10

nonlinear system described in (1) to evaluate the input voltage V_{in} for each molecule in the circuit during each propagation step τ [8].

$$V_{in,i}^\tau = V_{Dr,i}^\tau + \sum_{j \in IR} V_{j,i}^\tau (V_{in,j}^\tau, E_{ck,j}^\tau) \quad (1)$$

$V_{Dr,i}^\tau$ represents the influence of a driver cell on molecule i , and $V_{j,i}^\tau$ denotes the voltage generated by molecule j on molecule i . The molecular electrostatic interactions are considered inside an interaction radius, denoted as IR [27]. Each term $V_{j,i}$ depends on the specific clock value $E_{ck,j}^\tau$. In previous studies, SCERPA has been employed to design functional layouts for molFCN circuits [8], [18]. Importantly, molecules within the same clock regions were subjected to ideally uniform and vertical clock fields fixed at either -2 V/nm or +2 V/nm to force clock regions into Null or Hold states, thus neglecting field superpositions among the regions. Simulation accuracy should be increased

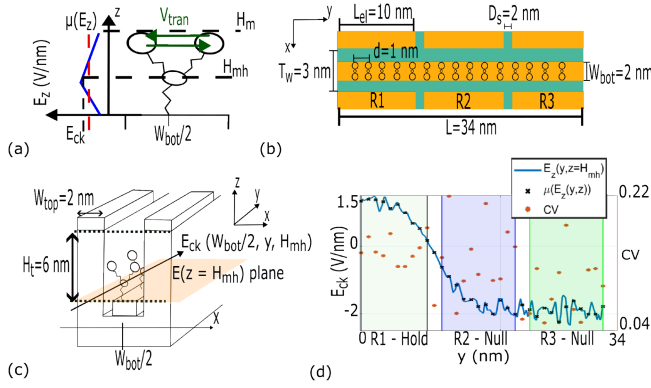


Fig. 3. (a) Definition of the E_{ck} -related relevant parameters and approximations. (b) Top view schematic of the three-phase wire. Molecules are aligned with constant intermolecular distance “ d ” along the ground electrode. The geometrical parameters are those of ConfA. (c) Perspective schematic of the nano-trench and E_{ck} extraction. (d) E_{ck} line during P1 along the three-phase wire in ConfA. The mean values of the fields along each molecule (black dots) follow the trend of the field values extracted at half the molecule height. Red spots represent the field coefficient of variation along each molecule.

by introducing realistic clock fields in the current algorithms to establish a link between the proposed molFCN hosting device and the circuit behavior. This study introduces an enhanced circuit simulation method, utilizing FEM simulations on molFCN devices to incorporate accurate clock fields. This approach verifies proper information propagation in the analyzed structure. Equation (2) presents the modified model this study introduces:

$$V_{in,i}^{\tau} = V_{Dr,i}^{\tau} + V_e^{\tau}(V_{el}^{\tau}) + \sum_{j \in IR} V_{j,i}^{\tau}(V_{in,j}^{\tau}, E_{ck,j}^{\tau}(V_{el}^{\tau})) \quad (2)$$

Two significant modifications are noteworthy. First, the $E_{ck,j}^{\tau}$ values for each molecule in the circuit are derived from FEM simulations and thus depend on the current electrode voltages V_{el}^{τ} . Therefore, this model overcomes the approximation of entire regions of molecules subjected to ideal clock fields and accounts for field superpositions among clock regions. Second, the effects of external transverse voltages V_e are introduced, especially to simulate realistic driving mechanisms, as will be clarified later in this study. The V_e depends on the electrode voltages V_{el} at the specific simulation step τ . Fig. 2(c) illustrates the simulation flow enabling the integration of FEM-derived quantities into the SCERPA algorithm. We use the SALOME tool to generate meshes for target devices, whereas ELMER implements the FEM calculations. The E_{ck} values at SCERPA-defined molecule positions in the circuit are extracted from the FEM-calculated field maps [28], [29]. Specifically, we make two essential considerations for the analysis, schematized in Fig. 3(a). First, each molecule E_{ck} is considered at a height corresponding to half the molecule height, labeled H_{mh} . We demonstrate this value to accurately measure the mean of the varying electric field E_z along molecules. Second, the transverse input voltage V_{tran} , i.e., V_e in (2), possibly caused by the electrodes is negligible provided the applications of equal V_{el} on the electrodes belonging to the same clock region and molecules anchored along the ground electrode mid-line.

Finally, SCERPA uses the evaluated E_{ck} while interpolating the available *ab initio*-derived VACTs corresponding to clock fields of -2 V/nm , $+2\text{ V/nm}$, and 0 V/nm to estimate the ACs specific to the E_{ck} influencing each molecule. Thus, a unique E_{ck} is associated with each molecule during each propagation step τ . The interpolation method permits rapid computations, bypassing *ab initio* simulations to estimate the VACTs under continuous clock field values.

III. RESULTS & DISCUSSION

This section analyzes various molFCN nano-trenches, highlighting the information propagation geometry dependencies. First, we define and justify the chosen nano-trench geometries and molecule pattern. Then, the analysis covers single-line three-phase wires (ConfA-ConfH) with varying nano-trench structures and addresses the criticalities of molFCN multi-line wires. Moreover, we evaluate a nano-trench circuit assembling a MV, a three-phase wire, and a T-connection. Finally, we demonstrate a realistic write-in mechanism.

A. Device Structure Definition

Fig. 3(b) and (c) show the basic geometry parameters of the analyzed device in one of the configurations analyzed in this section, i.e., confA. The geometrical sizes of all the proposed configurations are chosen according to technological evidences regarding the fabrication of nano-trenches, nano-electrodes and molecules patterning.

For nano-trenches, sub-3 nm trenches have been crafted using a self-shrinking mechanism in a dielectric material, as demonstrated in [20]. Additionally, sub-10 nm resolution has been achieved through electron-beam lithography with cold development on PMMA [19], [21]. Different solutions consider contact printing techniques to achieve sub-10 nm trenches on dielectric, as demonstrated in [30]. Furthermore, authors in [31] proposed nanoimprinting technology combined with atomic-layer deposition on hard and soft materials. For electrode patterning, existing literature has explored gold nanowires with dimensions as fine as 1.6 nm in radius and 10 nm in length [32], [33]. However, it's relevant to note that top electrode sizes minimally impacts electric field generation, as demonstrated in our preliminary work in [18]. Hence, alternative methods such as atomic layer deposition and electron beam lithography could be considered for electrode patterning [34], [35], [36]. Overall, molFCN fabrication could rely on the combination of advanced lithographic processes and molecules self-assembling, possibly avoiding atomic-scale manipulation necessary for other QCA implementations [37], [38].

We assume optimal deposition conditions concerning molecules, considering thiol depositions on atomically-flat gold metal and steric hindrance effects [39], [40], [41]. Concerning the substrate deposition, atomic-scale flatness must be considered both to minimize charge-related substrate effects and to ensure the sub-nm scale roughness required by molFCN to achieve correct information propagation [39], [42]. The design considerations for electrode dimensions in nano-trench are critical for ensuring stable information propagation, and setting the

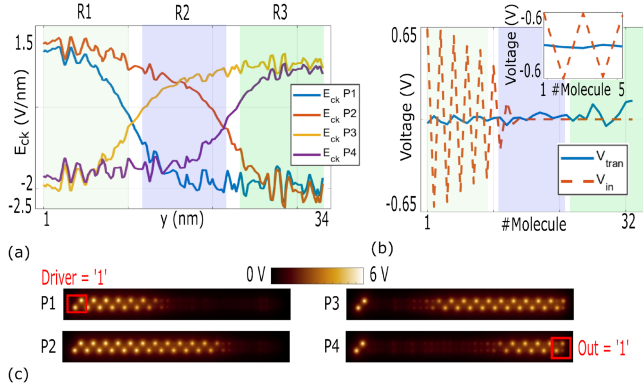


Fig. 4. (a) E_{ck} values in ConfA on the four phases. (b) Comparison between transverse voltages V_{tran} and the V_{in} generated by charge distributions evaluated by SCERPA. (c) Propagation analysis of a logic ‘1’ along the molFCN wire.

electrode length (L_{el}) to 10 nm balances fabrication ease and performance optimization. The chosen bottom electrode widths ensure a single-molecule line with ideal deposition along the ground electrode mid-line and a 2 nm steric hindrance width. Related to the proposed multi-line case, the trench and ground electrode widths enable two parallel lines of ideally deposited molecules. Additionally, variations in the inter-electrode distance (D_s) are studied to optimize device fabrication. W_{top} was chosen consistently with [18] to focus on the impact on the generated electric field. These design considerations are crucial for developing technologically scalable and robust molFCN circuits. Future research must balance factors such as parasitic capacitance, power dissipation, and fabrication challenges to assess streamlined design methodologies for nano-trench structures.

B. Nanotrenches for Three-Phase Wires Implementation

This section analyzes the device labeled as ConfA, whose geometrical parameters are shown in Fig. 3(b) (top view) and Fig. 3(c) (3D view). Molecules are aligned with an intermolecular distance equal to 1 nm along the ground electrode mid-line, namely $W_{bot}/2$ [18]. Table I reports the V_{el} controlling the information propagation during four propagation steps, named P1–P4. The blue line in Fig. 3(d) represents the E_{ck} along the ground electrode middle line at H_{mh} during P1. The chosen V_{el} cause an overall reduction of the fields in R1, making E_{ck} absolute values higher in Null than in the Hold conditions. We will refer to this situation as soft-activation. The black and red points in Fig. 3(d) report the field mean value and coefficient of variation (CV) for each molecule. The CV is evaluated as the ratio between the standard deviation and the mean value of E_z . The proximity of the average fields to the E_{ck} curve and low CV values validate the considered E_{ck} as a proper figure of merit. Fig. 4(a) reports the E_{ck} curves in P1–P4, obtained by applying the V_{el} in Table I. The V_{el} inducing the Null states are higher in magnitude than those providing the Hold condition, ensuring soft-activation. Fig. 4(b) confirms the negligible values of V_{tran} compared with the SCERPA-evaluated V_{in} on each molecule.

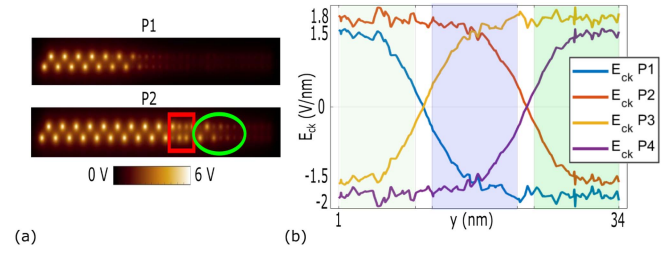


Fig. 5. (a) Propagation in ConfA when $V_{el} = \pm 8$ V are applied for Hold and Null states. Information aberration and unwanted activation are highlighted by red square and green circle, respectively. (b) E_{ck} values obtained by applying $V_{el} = \pm 8$ V on the electrodes for Hold and Null states in P1–P4.

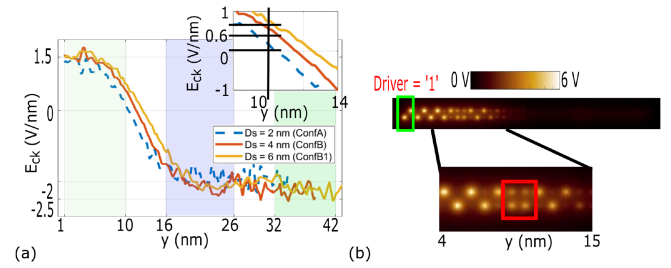


Fig. 6. (a) P1 E_{ck} for ConfA, ConfB and ConfB1. Zoom-in on the curves in the range from 10 nm to 14 nm. The higher D_s leads to higher fields in the regions between R1 and R2, thus decreasing the stability of the information propagation. (b) Information propagation analysis highlights information aberration for ConfB.

Furthermore, Fig. 4(c) reports the SCERPA-evaluated propagation. The bright spots identify the presence of positive charges evaluated by calculating the potential 0.2 nm above the Dot1 and Dot2 plane. The information stably propagates through the wire by soft-activations. To demonstrate the importance of soft-activation, Fig. 5 shows the results obtained by applying ± 8 V for Hold and Null conditions in P1–P4. The information aberration in Fig. 5(a) occurs due to the high fields influencing R2 and R3 during P2, shown in Fig. 5(b). Thus, an ineffective Null condition leads to random charge configuration on molecules in R3. Generally, soft-activation stabilizes information propagation in the presented nano-trench structure.

C. Information Propagation Geometry Dependencies

This section analyses the geometry dependences of the information propagation in nano-trenches. Table II lists the adopted structures. With reference to Fig. 3(b) and (c), the main parameters analyzed are the inter-electrode distance D_s , the trench width T_w , the bottom electrode width W_{bot} , the trench height H_t and the width of the top electrodes W_{top} . The electrodes length L_{el} is fixed to 10 nm unless otherwise specified. We analyze the most significant propagation phases for each configuration, applying the V_{el} in Table I.

1) Inter-Electrode Distance: Fig. 6(a) compares the E_{ck} in P1 for ConfA, ConfB and ConfB1. Fig. 6(b) shows that information aberration occurs using ConfB. Indeed, the fields in the inter-electrode regions are higher for increasing D_s ,

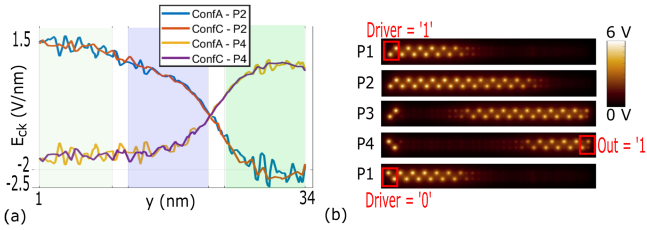


Fig. 7. (a) Comparison between P2 and P4 for ConfA and ConfC. The curves superimpose, indicating molFCN robustness to slight trench width variations. (b) Propagation with ConfC. The propagation is correct, and the chosen V_{el} permits pipelining.

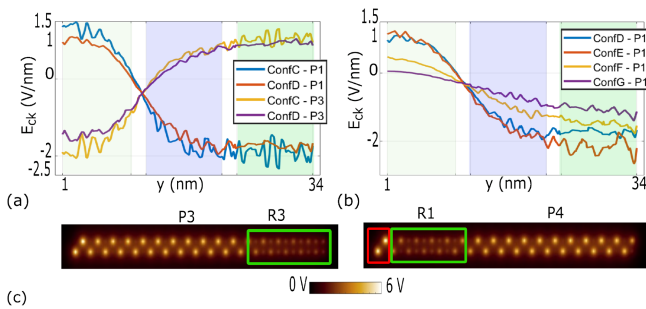


Fig. 8. (a) Comparison between P1 and P3 for ConfC and ConfD. (b) H_t variation effect on the E_{ck} during P1. (c) Propagation in P3 (left) and P4 (right) for ConfG. Green rectangles highlight unstable Null conditions.

leading to a weaker Null condition on those molecules. Consequently, charges switch randomly due to the V_{in} generated by the molecules in R1. The random molecules switch in the inter-electrode region causes back-propagation information aberration in R1. Generally, the higher D_s , the higher the number of molecules in the inter-electrodes regions, leading to loss of the clock control feature and increasing aberration probability. The result shows the importance of considering and controlling the inter-electrode separation during the molFCN device fabrication.

2) *Trench Width:* Fig. 7(a) compares E_{ck} values during P2 and P4 for ConfA and ConfC. The curves are almost perfectly superimposed, apart from oscillation related to the adopted meshes granularity, demonstrating molFCN robustness to slight T_w variations. Fig. 7(b) shows correct information propagation using ConfC. Moreover, it reports P1 of a possible second propagation, demonstrating the proposed methodology permits pipelined simulation analysis. Multi-line circuits must be considered for higher T_w .

3) *Top Electrodes Width and Trench Height:* We now analyze variations of H_t and W_{top} by modifying ConfC. Increasing the trench height causes the E_{ck} reduction. Fig. 8(a) compares the fields for ConfC and ConfD, showing a slight E_{ck} decrease for this small H_t increase. Fig. 8(b) deepens the analysis of H_t and W_{top} parametrization. In particular, the variation of W_{top} from 2 nm to 6 nm, i.e., moving from ConfD to ConfE, has a sensible influence on the E_{ck} values, as shown by the red and blue curves in Fig. 8(b). The higher clock values in R3 adopting ConfE lead to a stronger reset state for those molecules,

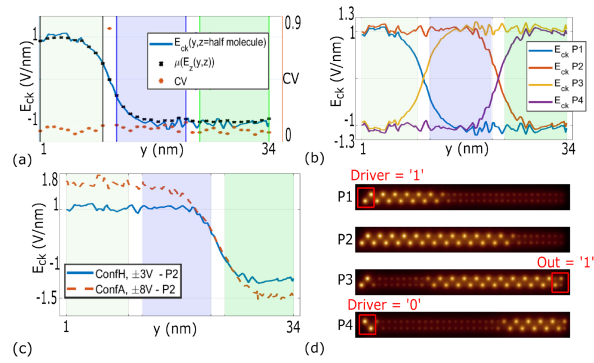


Fig. 9. (a) Validation of the E_{ck} approximation for ConfH. (b) E_{ck} values extracted for ± 3 V applied to obtain Hold and Null states in ConfH. (c) Comparison between P2 for ConfA and ConfH. (d) Propagation analysis in the ConfH nano-trench.

attributed to the larger electrode surface in the ConfD case, where W_{top} equals 6 nm. Consequently, the propagation stability increases thanks to the enhanced clock control, reducing the charge in Dot1 and Dot2 in reset state regions, as reported in Fig. 2 in the SI. Moreover, Fig. 3 in SI compares E_{ck} for ConfD and ConfE in P1–P4, whereas Fig. 4 demonstrates the correct propagation of Logic ‘0’ and ‘1’ for both ConfD and ConfE. This finding underscores the potential benefits of increasing electrode surface area for achieving more stable resets, thereby easing fabrication requirements for clock electrodes on top of the trench. Furthermore, the curves in Fig. 8(b) confirm the E_{ck} decrease for increasing H_t . Indeed, E_{ck} for ConfG in P1 ranges close to 0 V/nm. The E_{ck} reduction affects all the phases, leading to unstable situations. In particular, Fig. 8(c) reports the charge distribution during P3 and P4 for ConfG, highlighting unstable Null conditions in R3 and R1. Despite fabrication constraints reduction, deep trenches could be a valuable solution for molFCN only by introducing a consistent V_{el} increase, thus increasing power consumption. Differently, lowering H_t as in ConfH reduces the needed V_{el} to obtain proper E_{ck} . Fig. 9(a) demonstrates that the E_{ck} well-represent the fields along each molecule, renewing the E_{ck} measure validation. Fig. 9(b) reports the E_{ck} profiles considering $V_{el} = \pm 3$ V for Hold and Null states in ConfH. Interestingly, the curves resemble those in Fig. 5(b), which is reasonable given the use of opposite signs and equal magnitude voltages in both cases. Fig. 9(c) compares the E_{ck} curves during P2 already shown in Figs. 9(b) and 5(b). Combining ConfH with $V_{el} = \pm 3$ V provides lower fields in R2, leading to lower ACs and reducing the V_{in} influencing molecules in R3. Thus, the Null condition in R3 is effective and guarantees stable propagation, as Fig. 9(d) reports. These results demonstrate stable information propagation by applying low V_{el} , which is mandatory for future molFCN device integration. The condition is achieved using a low H_t trench, thus reducing power consumption at the expense of more strict fabrication requirements.

D. Two-Line Wire Analysis

Multi-line devices can be embraced to relax nano-trench fabrication specifications and improve molFCN circuit robustness

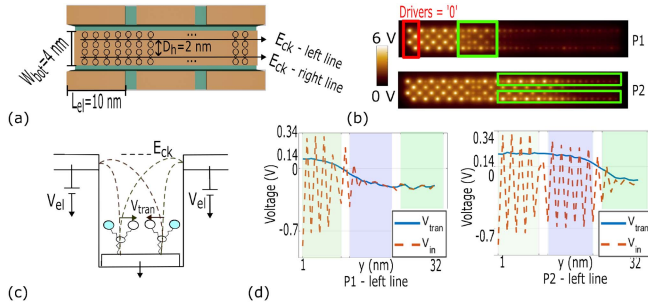


Fig. 10. (a) Schematic of the nano-trench two-line wire. Molecules are positioned along two parallel lines on the ground electrode. The lines are separated by $D_h = 2 \text{ nm}$ with respect to the molecules centers. (b) Propagation analysis. The green rectangle in the top figure highlights the information clash. Green rectangles in the bottom figure highlight the effect of V_{tran} on molecules. (c) Schematic representation of the V_{tran} generation leading to charge localization in the external dots. (d) Comparison V_{in} - V_{tran} on the wire left line during P1 (left) and P2 (right). The not-negligible V_{tran} causes the V_{in} to differ from zero along the whole wire.

TABLE III
VOLTAGES APPLIED TO R1, R2, AND R3 IN THE TWO-LINE NANO-TRENCH

Region	Electrode Voltage V_{el}			
	P1	P2	P3	P4
R1	-6 V	-6 V	+8 V	+8 V
R2	+8 V	-6 V	-6 V	+8 V
R3	+8 V	+8 V	-6 V	-6 V

to missing cell defects and spurious crosstalk effects, particularly affecting fundamental logic gates such as the inverter [8], [9], [18], [43]. Therefore, this section analyses the nano-trench structure of a two-line wire, shown in Fig. 10(a), to preliminary evaluate the applicability of multi-line devices in nano-trench devices. The E_{ck} are measured along the mid-line of each row of molecules at a height corresponding to H_{mh} . We simulate four phases, applying the V_{el} in Table III. Fig. 10(b) shows the SCERPA result, reporting information aberration.

In this case, as Fig. 10(c) schematizes, the molecules are not positioned along the center of the nano-trench and non-negligible V_{tran} deriving from not-null transverse field components occurs, moving charges toward the dots external to the wire center, as shown by Fig. 10(b). Specifically, Fig. 10(d) compares the V_{in} and the V_{tran} voltages during P1 and P2 along the left line. The net non-zero V_{tran} provides a not null V_{in} to each molecule, guiding charge distribution even in Null-state regions. Hence, we identify for the first time that transverse fields represent an issue for molFCN multi-line circuits. Consequently, multi-line molFCN circuits need structures ensuring uniform and vertical clock fields, thus minimizing V_{tran} effects. Future works will investigate in-depth multi-line molFCN, also analyzing electrode solutions generating vertical clock fields.

E. Logic Circuit Analysis

This section applies the proposed methodology to a molFCN logic circuit presenting ConfC geometries and reported in Fig. 11(a). The circuit comprises a MV (R1-R3), a 3-phase wire (R4-R6), and a T-connection (fan-out) (R7-R8). The intermolecular distances are 2 nm and 1 nm along x and y ,

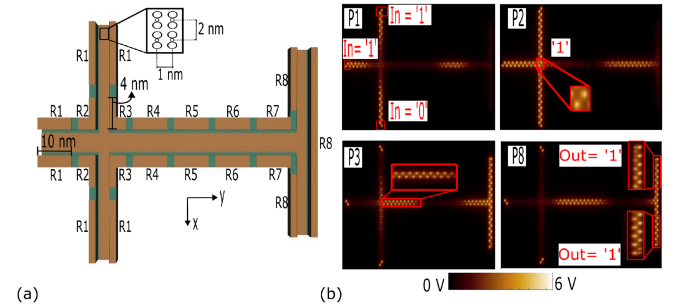


Fig. 11. (a) Logic circuit schematic. (b) The information moves during P1 in the MV input branches (top-left). Then, the MV elaborates the information, providing the correct logic output (top-right). The computed value propagates in the output three-phase wire (bottom-left) and finally reaches the two ends of the T-connection (bottom-right) after a latency determined by the number of clock regions.

TABLE IV
VOLTAGE VALUES APPLIED IN THE PROPAGATION PHASES ON THE CIRCUIT IN FIG. 11(A)

Region	Electrode Voltage V_{el}				
	P1	P2&P6	P3&P7	P4&P8	P5
R1	-8 V	-10 V	+10 V	+10 V	-8 V
R2	+10 V	-5 V	+8 V	10 V	+10 V
R3	+10 V	+3 V	-5 V	+10 V	+10 V
R4	+10 V	+8 V	-3 V	-10 V	+12 V
R5	+10 V	+12 V	+12 V	-3 V	-8 V
R6	-5 V	-4 V	+10 V	+12 V	-3 V
R7	+10 V	-3 V	-4 V	+10 V	+12 V
R8	+10 V	+12 V	-10 V	-10 V	+10 V

respectively. We simulate the circuit in eight phases, P1–P8, to account for propagation latency. Table IV reports the chosen V_{el} , which ensure soft-activation conditions. Fig. 11(b) reports the propagation results, considering two logic ‘1’ and a logic ‘0’ as inputs to the MV. First, the inputs propagate through the MV input wires during P1. Then, two sets of electrodes, R2 and R3, guarantee correct MV input-output synchronization in P2 and P3, necessary for correct information elaboration [18]. The circuit outputs in P8 are logic ‘1’, thus confirming the correct information propagation along the wire and the fan-out. This example validates the previously analyzed structures and the proposed method suitable for designing logic nano-trench-based molFCN circuits. Additionally, different input combinations are detailed in the SI file, explicitly showing the 101, 010, and 001 cases. Overall, the values in Table IV ensure stable information propagation and can be considered suitable for laboratory prototype molFCN validation. Future work aims to simplify clock signal application and optimize electrode layout to reduce chip-level metallization requirements and circuit complexity.

F. Driver Mode Addressing

In molFCN devices, the charge distribution must be fixed by an external input voltage V_{ext} on a set of molecules to achieve the driving mechanism [44], [45]. Fig. 12(a) shows a three-phase wire with two additional electrodes connected to V_L and V_R and schematizes the driving mechanism. The potential difference $V_L - V_R$ generates the V_{ext} on the driver molecules. Notably, the

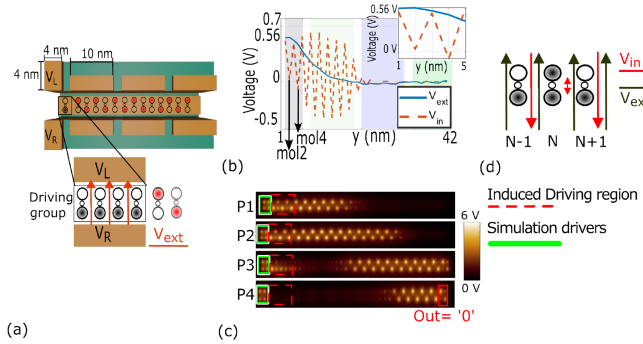


Fig. 12. (a) Nano-trench structure embedding driving electrodes and driving mechanism schematic. (b) P1 V_{in} and V_{ext} comparison in ConfC adjusted for driving mode. (c) Propagation analysis: the V_{ext} -induced driving region is poorly defined for $H_t = 6 \text{ nm}$. The SCERPA simulation drivers, highlighted in the green boxes, are turned off. (d) V_{in} and V_{ext} balance on molecules. Similar magnitude V_{in} and V_{ext} contributions lead to negligible molecule charge distribution.

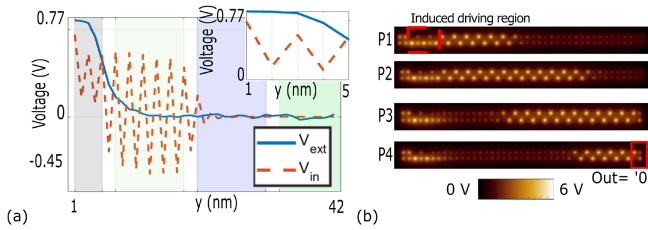


Fig. 13. (a) P1 V_{in} and V_{ext} comparison using ConfH geometries. The net V_{in} values are not zero for ConfH. (b) Propagation analysis: using confH, the driving region (green rectangle in the upper image) is well-defined.

transverse electric field, arising from the potential difference between the driver electrodes, extends across the molecular wire. Accurate considerations of V_{ext} on the molecules in the wire are essential to obtain the desired logical information propagation. Furthermore, V_{ext} must be set to concurrently ensure Hold and driving conditions.

We now simulate the propagation along three-phase wires by varying electrode voltages and the configuration, using V_{ext} values as V_e^T and fixing $V_{Dr,i}^T$ to 0 in (2). We consider the V_{el} on R1, R2, and R3 in Table I, $V_L = 3 \text{ V}$, $V_R = -10 \text{ V}$, and ConfC geometries. Fig. 12(b) compares molecule V_{in} calculated by SCERPA with the applied V_{ext} in P1. The V_{ext} guides the charge distributions on the molecules in the driving region, forcing V_{in} to range from 0.5 V down to 0 V. Fig. 12(c) shows the propagation. With this configuration there is no well-defined set of driver molecules, introducing possible instabilities into the circuit. Indeed, as Fig. 12(d) explains, the charges on molecule N move to minimize Coulomb's repulsion with charges on molecule N-1. Concurrently, V_{ext} drives the charges on the molecule N in the opposite direction. The result is a null charge distribution, thus justifying the $V_{in} = 0 \text{ V}$ on molecules 2 and 4 in Fig. 12(b). Increasing the difference between V_L and V_R to enhance the V_{ext} increases the charge polarization in the driving region. However, a too-high potential difference would also influence the other molecules in the wire, thus causing instabilities. Better behavior is obtained by considering ConfH

geometries, $\pm 3 \text{ V}$ for Hold and Null states, and -5 V and $+1 \text{ V}$ as V_R and V_L , respectively. Fig. 13(a) highlights the higher V_{ext} in P1, which overcomes the V_{in} and drives same-direction charge confinement on the driver molecules, overall ensuring stable propagation, reported in Fig. 13(b). These simulations highlight the need to overcome charge self-arrangement to achieve the driving mechanism, and the results are significant in addressing a valuable solution for future molFCN prototypes.

IV. CONCLUSION

This work integrates molecular and device physics to enhance molFCN simulation realism. FEM calculations are used to analyze clock fields in nano-trenches with various geometries. The SCERPA tool evaluated information propagation in molFCN circuits based on the FEM-calculated electric fields. Specifically, we designed voltages permitting information propagation in single-line three-phase wires, two-line wires, and logic circuits. The results demonstrate the nano-trench is a valuable solution for molFCN prototypes, enabling information processing in the circuit layout. We showcased low-voltage applications by employing low-height trenches. This solution preserves clock control features, reduces power consumption, and proves beneficial when using bis-ferrocenes. The methodology is generalizable to molFCN devices involving alternative molecules, potentially requiring lower polarization fields. The two-line wire analyses highlighted the need for uniform vertical fields to prevent propagation anomalies caused by transverse voltages. Additionally, we examined realistic driving mechanisms in a three-phase wire. The results emphasized the necessity for external voltages to overcome Coulomb's repulsion conditions. Low-height nano-trenches facilitate stable and low-voltage drivers. Overall, this paper addresses molFCN prototyping using FEM calculations and SCERPA for device-physics-aware analysis. Future work will explore time-dependent voltages in molFCN propagation modeling to introduce power consumption and scalability analysis of nano-trench devices for molFCN. Time-domain considerations will provide insightful comparisons with current state-of-the-art logic gates time sensitivity. Moreover, fabrication results will be incorporated into the simulation framework to enhance simulation accuracy further.

REFERENCES

- [1] C. S. Lent, B. Isaksen, and M. Lieberman, "Molecular quantum-dot cellular automata," *J. Amer. Chem. Soc.*, vol. 125, no. 4, pp. 1056–1063, 2003.
- [2] R. M. Macrae, "Mixed-valence realizations of quantum dot cellular automata," *J. Phys. Chem. Solids*, vol. 177, 2023, Art. no. 111303.
- [3] N. Liza, D. Murphrey, P. Cong, D. W. Beggs, Y. Lu, and E. P. Blair, "Asymmetric, mixed-valence molecules for spectroscopic readout of quantum-dot cellular automata," *Nanotechnol.*, vol. 33, no. 11, 2021, Art. no. 115201.
- [4] J. A. Christie et al., "Synthesis of a neutral mixed-valence diferrocenyl carborane for molecular quantum-dot cellular automata applications," *Angewandte Chemie Int. Ed.*, vol. 54, no. 51, pp. 15448–15451, 2015.
- [5] V. Arima et al., "Toward quantum-dot cellular automata units: Thiolated-carbazole linked bisferrocenes," *Nanoscale*, vol. 4, no. 3, pp. 813–823, 2012.
- [6] Y. Ardesi, A. Pulimeno, M. Graziano, F. Riente, and G. Piccinini, "Effectiveness of molecules for quantum cellular automata as computing devices," *J. Low Power Electron. Appl.*, vol. 8, no. 3, 2018, Art. no. 24.

- [7] C. S. Lent, M. Liu, and Y. Lu, "Bennett clocking of quantum-dot cellular automata and the limits to binary logic scaling," *Nanotechnol.*, vol. 17, no. 16, 2006, Art. no. 4240.
- [8] Y. Ardesi, G. Turvani, M. Graziano, and G. Piccinini, "SCERPA simulation of clocked molecular field-coupling nanocomputing," *IEEE Trans. Very Large Scale Integration Syst.*, vol. 29, no. 3, pp. 558–567, Mar. 2021.
- [9] J. Timler and C. S. Lent, "Power gain and dissipation in quantum-dot cellular automata," *J. Appl. Phys.*, vol. 91, no. 2, pp. 823–831, 2002.
- [10] E. P. Blair, E. Yost, and C. S. Lent, "Power dissipation in clocking wires for clocked molecular quantum-dot cellular automata," *J. Comput. Electron.*, vol. 9, pp. 49–55, 2010.
- [11] Y. Wang and M. Lieberman, "Thermodynamic behavior of molecular-scale quantum-dot cellular automata (QCA) wires and logic devices," *IEEE Trans. Nanotechnol.*, vol. 3, no. 3, pp. 368–376, Sep. 2004.
- [12] Y. Ardesi, A. Gaeta, G. Beretta, G. Piccinini, and M. Graziano, "AB initio molecular dynamics simulations of field-coupled nanocomputing molecules," *J. Integr. Circuits Syst.*, vol. 16, no. 1, pp. 1–8, 2021.
- [13] E. P. Blair, S. A. Corcelli, and C. S. Lent, "Electric-field-driven electron-transfer in mixed-valence molecules," *J. Chem. Phys.*, vol. 145, no. 1, pp. 014307-1–014307-12, 2016.
- [14] M. Niemier et al., "Nanomagnet logic: Progress toward system-level integration," *J. Phys., Condens. Matter*, vol. 23, no. 49, 2011, Art. no. 493202.
- [15] M. S. Fashami, K. Munira, S. Bandyopadhyay, A. W. Ghosh, and J. Atulasimha, "Switching of dipole coupled multiferroic nanomagnets in the presence of thermal noise: Reliability of nanomagnetic logic," *IEEE Trans. Nanotechnol.*, vol. 12, no. 6, pp. 1206–1212, Nov. 2013.
- [16] A. O. Orlov, I. Amlani, G. H. Bernstein, C. S. Lent, and G. L. Snider, "Realization of a functional cell for quantum-dot cellular automata," *Science*, vol. 277, no. 5328, pp. 928–930, 1997.
- [17] I. Amlani, A. O. Orlov, G. Toth, G. H. Bernstein, C. S. Lent, and G. L. Snider, "Digital logic gate using quantum-dot cellular automata," *Science*, vol. 284, no. 5412, pp. 289–291, 1999.
- [18] Y. Ardesi, U. Garlando, F. Riente, G. Beretta, G. Piccinini, and M. Graziano, "Taming molecular field-coupling for nanocomputing design," *ACM J. Emerg. Technol. Comput. Syst.*, vol. 19, no. 1, pp. 1–24, 2022.
- [19] W. Hu, K. Sarveswaran, M. Lieberman, and G. H. Bernstein, "High-resolution electron beam lithography and DNA nano-patterning for molecular QCA," *IEEE Trans. Nanotechnol.*, vol. 4, no. 3, pp. 312–316, May 2005.
- [20] P.-S. Yang, P.-H. Cheng, C. R. Kao, and M.-J. Chen, "Novel self-shrinking mask for sub-3 nm pattern fabrication," *Sci. Rep.*, vol. 6, no. 1, 2016, Art. no. 29625.
- [21] W. Hu, K. Sarveswaran, M. Lieberman, and G. H. Bernstein, "Sub-10 nm electron beam lithography using cold development of poly (methyl-methacrylate)," *J. Vac. Sci. Technol. B, Microelectronics Nanometer Structures Process. Meas. Phenomena*, vol. 22, no. 4, pp. 1711–1716, 2004.
- [22] A. J. Mackus, M. J. Merkx, and W. M. Kessels, "From the bottom-up: Toward area-selective atomic layer deposition with high selectivity," *Chem. Mater.*, vol. 31, no. 1, pp. 2–12, 2018.
- [23] A. Mackus, A. Bol, and W. Kessels, "The use of atomic layer deposition in advanced nanopatterning," *Nanoscale*, vol. 6, no. 19, pp. 10941–10960, 2014.
- [24] S. S. H. Ng et al., "SIQAD: A design and simulation tool for atomic silicon quantum dot circuits," *IEEE Trans. Nanotechnol.*, vol. 19, pp. 137–146, 2020.
- [25] E. Pensa et al., "The chemistry of the sulfur–gold interface: In search of a unified model," *Accounts Chem. Res.*, vol. 45, no. 8, pp. 1183–1192, 2012.
- [26] G. Beretta, Y. Ardesi, G. Piccinini, and M. Graziano, "vlsi-nanocomputing/scerpa: Scerpa v4.0.1" 2022. [Online]. Available: <https://zenodo.org/record/7457038>
- [27] Y. Ardesi, R. Wang, G. Turvani, G. Piccinini, and M. Graziano, "SCERPA: A self-consistent algorithm for the evaluation of the information propagation in molecular field-coupled nanocomputing," *IEEE Trans. Comput.-Aided Des. Integr. Circuits Syst.*, vol. 39, no. 10, pp. 2749–2760, Oct. 2019.
- [28] V. Bergeaud and V. Lefebvre, "Salome a software integration platform for multi-physics, pre-processing and visualisation," 2010.
- [29] M. Malinen and P. Råback, "Elmer finite element solver for multiphysics and multiscale problems," *Multiscale Model. Methods Appl. Mater. Sci.*, vol. 19, pp. 101–113, 2013.
- [30] Y. Wang, X. Liang, Y. Liang, and S. Y. Chou, "Sub-10-nm wide trench, line, and hole fabrication using pressed self-perfection," *Nano Lett.*, vol. 8, no. 7, pp. 1986–1990, 2008.
- [31] J. Y. Woo, S. Jo, J. H. Oh, J. T. Kim, and C.-S. Han, "Facile and precise fabrication of 10-nm nanostructures on soft and hard substrates," *Appl. Surf. Sci.*, vol. 484, pp. 317–325, 2019.
- [32] A. Halder and N. Ravishankar, "Ultrafine single-crystalline gold nanowire arrays by oriented attachment," *Adv. Mater.*, vol. 19, no. 14, pp. 1854–1858, 2007.
- [33] N. Pazos-Pérez, D. Baranov, S. Irsen, M. Hilgendorff, L. M. Liz-Marzán, and M. Giersig, "Synthesis of flexible, ultrathin gold nanowires in organic media," *Langmuir*, vol. 24, no. 17, pp. 9855–9860, 2008.
- [34] R. McMullen, A. Mishra, and J. D. Slinker, "Straightforward fabrication of sub-10 nm nanogap electrode pairs by electron beam lithography," *Precis. Eng.*, vol. 77, pp. 275–280, 2022.
- [35] M. B. Griffiths, P. J. Pallister, D. J. Mandia, and S. T. Barry, "Atomic layer deposition of gold metal," *Chem. Mater.*, vol. 28, no. 1, pp. 44–46, 2016.
- [36] M. Makela, T. Hatanpaa, K. Mizohata, J. Raisanen, M. Ritala, and M. Leskela, "Thermal atomic layer deposition of continuous and highly conducting gold thin films," *Chem. Mater.*, vol. 29, no. 14, pp. 6130–6136, 2017.
- [37] R. A. Wolkow et al., "Silicon atomic quantum dots enable beyond-CMOS electronics," *Field-Coupled Nanocomputing, Paradigms, Progress, Perspectives*, vol. 8280, pp. 33–58, 2014.
- [38] R. Achal et al., "Lithography for robust and editable atomic-scale silicon devices and memories," *Nature Commun.*, vol. 9, no. 1, 2018, Art. no. 2778.
- [39] M. Graziano, R. Wang, M. R. Roch, Y. Ardesi, F. Riente, and G. Piccinini, "Characterisation of a bis-ferrocene molecular QCA wire on a non-ideal gold surface," *Micro Nano Lett.*, vol. 14, no. 1, pp. 22–27, 2019.
- [40] C. Vericat et al., "Self-assembled monolayers of thiolates on metals: A review article on sulfur-metal chemistry and surface structures," *Rsc Adv.*, vol. 4, no. 53, pp. 27730–27754, 2014.
- [41] H. Kim, J. K. Saha, Z. Zhang, J. Jang, M. A. Matin, and J. Jang, "Molecular dynamics study on the self-assembled monolayer grown from a droplet of alkanethiol," *J. Phys. Chem. C*, vol. 118, no. 20, pp. 11149–11157, 2014.
- [42] J.-S. Huang et al., "Atomically flat single-crystalline gold nanostructures for plasmonic nanocircuitry," *Nature Commun.*, vol. 1, no. 1, 2010, Art. no. 150.
- [43] Y. Ardesi, G. Beretta, M. Vacca, G. Piccinini, and M. Graziano, "Impact of molecular electrostatics on field-coupled nanocomputing and quantum-dot cellular automata circuits," *Electronics*, vol. 11, no. 2, 2022, Art. no. 276.
- [44] A. Pulimenò, M. Graziano, C. Abrardi, D. Demarchi, and G. Piccinini, "Molecular QCA: A write-in system based on electric fields," in *Proc. IEEE 4th Int. NanoElectronics Conf.*, 2011, pp. 1–2.
- [45] E. Blair, "Electric-field inputs for molecular quantum-dot cellular automata circuits," *IEEE Trans. Nanotechnol.*, vol. 18, pp. 453–460, 2019.